9. T. J. Buschman, E. K. Miller, *Science* **315**, 1860–1862 (2007).
10. G. G. Gregoriou, S. J. Gotts, H. Zhou, R. Desimone, *Science* **324**, 1207–1210 (2009).
11. T. Moore, K. M. Armstrong, *Nature* **421**, 370–373 (2003).
12. B. Noudoost, T. Moore, *Nature* **474**, 372–375 (2011).
13. L. B. Ekstrom, P. R. Roelfsema, J. T. Arsenault, G. Bonmassar, W. Vanduffel, *Science* **321**, 414–417 (2008).
14. Y. Chen *et al.*, *Nat. Neurosci.* **11**, 974–982 (2008).
15. K. A. Sundberg, J. F. Mitchell, J. H. Reynolds, *Neuron* **61**, 952–963 (2009).
16. K. McAlonan, J. Cavanaugh, R. H. Wurtz, *Nature* **456**, 391–394 (2008).
17. G. Purushothaman, R. Marion, K. Li, V. A. Casagrande, *Nat. Neurosci.* **15**, 905–912 (2012).
18. M. Sarter, M. E. Hasselmo, J. P. Bruno, B. Givens, *Brain Res. Brain Res. Rev.* **48**, 98–111 (2005).
19. Y. B. Saalmann, M. A. Pinsk, L. Wang, X. Li, S. Kastner, *Science* **337**, 753–756 (2012).
20. M. A. Segraves, M. E. Goldberg, *J. Neurophysiol.* **58**, 1387–1419 (1987).
21. The projection to superior colliculus arises only from deep layers (Fig. 1D), similar to that in primate FEF.
22. S. Treue, J. C. Martínez Trujillo, *Nature* **399**, 575–579 (1999).
23. T. Moore, M. Fallah, *J. Neurophysiol.* **91**, 152–162 (2004).
24. X. Xu, K. D. Roby, E. M. Callaway, *J. Comp. Neurol.* **518**, 389–404 (2010).
25. G. Fishell, B. Rudy, *Annu. Rev. Neurosci.* **34**, 535–567 (2011).
26. H. Adesnik, W. Bruns, H. Taniguchi, Z. J. Huang, M. Scanziani, *Nature* **490**, 226–231 (2012).
27. S. H. Lee *et al.*, *Nature* **488**, 379–383 (2012).
28. N. R. Wilson, C. A. Runyan, F. L. Wang, M. Sur, *Nature* **488**, 343–348 (2012).
29. L. Petreanu, T. Mao, S. M. Sternson, K. Svoboda, *Nature* **457**, 1142–1145 (2009).
30. I. R. Wickersham *et al.*, *Neuron* **53**, 639–647 (2007).
31. S. Lee, I. Kruglikov, Z. J. Huang, G. Fishell, B. Rudy, *Nat. Neurosci.* **16**, 1662–1670 (2013).
32. L. Madisen *et al.*, *Nat. Neurosci.* **15**, 793–802 (2012).
33. Y. Fu *et al.*, *Cell* **156**, 1139–1152 (2014).
34. C. K. Pfeffer, M. Xue, M. He, Z. J. Huang, M. Scanziani, *Nat. Neurosci.* **16**, 1068–1076 (2013).
35. H. J. Pi *et al.*, *Nature* **503**, 521–524 (2013).
36. J. F. Mitchell, K. A. Sundberg, J. H. Reynolds, *Neuron* **55**, 131–141 (2007).
37. Based on a magnification factor of 10 μm per degree in mouse V1 (*42*), 200 μm of cortical distance corresponds to 20° of visual angle. A previous study (*26*) showed that for most neurons, the preferred size of visual stimulus was <15° in radius, and stimuli beyond this radius suppressed neuronal responses. This suggests that surround suppression for top-down modulation and bottom-up processing occur on similar spatial scales. The same inhibitory circuits could also contribute to decreased receptive field similarity and signal correlation between V1 neurons over ~200 μm (*42*).
38. J. J. Letzkus *et al.*, *Nature* **480**, 331–335 (2011).
39. X. Jiang, G. Wang, A. J. Lee, R. L. Stornetta, J. J. Zhu, *Nat. Neurosci.* **16**, 210–218 (2013).
40. S. P. Mysore, E. I. Knudsen, *Nat. Neurosci.* **16**, 473–478 (2013).
41. S. Ardid, X. J. Wang, A. Compte, *J. Neurosci.* **27**, 8486–8495 (2007).
42. V. Bonin, M. H. Histed, S. Yurgenson, R. Clay Reid, *J. Neurosci.* **31**, 18506 (2011).

OCEANOGRAPHY

Centennial changes in North Pacific anoxia linked to tropical trade winds

Curtis Deutsch,[1]* William Berelson,[2] Robert Thunell,[3] Thomas Weber,[1] Caitlin Tems,[2] James McManus,[4]† John Crusius,[5] Taka Ito,[6] Timothy Baumgartner,[7] Vicente Ferreira,[7] Jacob Mey,[8,9] Alexander van Geen[8]

Climate warming is expected to reduce oxygen (O_2) supply to the ocean and expand its oxygen minimum zones (OMZs). We reconstructed variations in the extent of North Pacific anoxia since 1850 using a geochemical proxy for denitrification ($\delta^{15}N$) from multiple sediment cores. Increasing $\delta^{15}N$ since ~1990 records an expansion of anoxia, consistent with observed O_2 trends. However, this was preceded by a longer declining $\delta^{15}N$ trend that implies that the anoxic zone was shrinking for most of the 20th century. Both periods can be explained by changes in winds over the tropical Pacific that drive upwelling, biological productivity, and O_2 demand within the OMZ. If equatorial Pacific winds resume their predicted weakening trend, the ocean's largest anoxic zone will contract despite a global O_2 decline.

Below the ocean's surface, the decomposition of sinking detritus creates a layer of low-O_2 water inhospitable to many marine species (*1*). These oxygen minimum zones (OMZs) are predicted to expand with climate warming (*2, 3*), causing a major disruption to ecosystems, especially in areas where OMZ waters impinge on coastal environments already under low-O_2 stress from natural or human causes (*4–6*). This putative expansion stems from two direct consequences of climate change: As the surface ocean warms, its gas solubility and density both decrease, reducing the concentration of O_2 in surface water and the rate at which that water is transported downward against a more stable stratification. The resulting decline in O_2 supply to the ocean interior is generally supported by observed trends toward lower O_2 over the past few decades, over many parts of the world's oceans (*7*), including the strong OMZs in the tropics (*8*).

The climatic response of the OMZ also depends on O_2 demand, although the factors governing those biological rates are less well understood. Earth system model simulations project large future decreases in the sinking flux of organic matter throughout the tropics (*9*), which should reduce O_2 demand in the OMZ, counteracting

[1]School of Oceanography, University of Washington, Seattle, WA, USA. [2]Department of Earth Sciences, University of Southern California, Los Angeles, CA, USA. [3]Department of Earth and Ocean Sciences, University of South Carolina, Columbia, SC, USA. [4]College of Earth, Ocean, and Atmospheric Sciences, Oregon State University, Corvallis, OR, USA. [5]U.S. Geological Survey, University of Washington School of Oceanography, Seattle, WA, USA. [6]School of Earth and Atmospheric Sciences, Georgia Institute of Technology, Atlanta, GA, USA. [7]Departamento de Oceanografía Biológica, Centro de Investigación Científica y de Educación Superior de Ensenada, Baja California, México. [8]Lamont-Doherty Earth Observatory of Columbia University, Palisades, NY, USA. [9]Department of Physical Sciences, Kingsborough Community College, City University of New York, New York, NY, USA.
*Corresponding author. E-mail: cdeutsch@uw.edu †Present address: Department of Geosciences, University of Akron, Akron, OH, USA.

the loss of O_2 supply. In the eastern tropical and subtropical Pacific Ocean, the OMZ variability over the last 50 years appears to have been driven primarily by O_2 demand, which is strongly modulated by decadal climate variability (*10, 11*). In light of that variability, the instrumental O_2 record is still sparse and short, making long-term trends in the OMZ difficult to detect or attribute especially in the most intense tropical OMZs in the Pacific and Indian oceans (*8, 12*). The relative strength of future changes in O_2 supply versus demand in the tropical OMZ would be clearer if their long-term response to the climate warming since the industrial revolution were known.

We reconstructed changes in the OMZ of the eastern tropical northern Pacific (ETNP) over the past 150 years using a geochemical proxy for water column anoxia that is recorded in sediments (Fig. 1). At the eastern terminus of the OMZ, where thermocline waters shoal toward the productive surface layer, respiration depletes O_2 and anaerobic bacteria begin reducing nitrate (NO_3^-) to oxidize organic matter (*13*) (Fig. 1). This denitrification process preferentially removes the lighter ^{14}N isotope of N, leaving a residual NO_3^- pool enriched in heavier ^{15}N (*14, 15*). The resulting nitrate with a high isotope ratio, $\delta^{15}N$ [$\delta^{15}N = (^{15}N/^{14}N)/R_{air} - 1) \times 1000$, where R_{air} is the N isotope ratio in air], is upwelled to the surface, where it can be transferred to plankton communities and then, via sinking particles, into sediments (*16, 17*). In regions with complete consumption of upwelled nitrate, the $\delta^{15}N$ of particulate organic nitrogen (PON) accumulating on the sea floor closely resembles that of nitrate in waters at ~100 m (*18*). In the absence of postdepositional alteration, downcore variations in $\delta^{15}N$ provide a history of the integrated rates of denitrification and the size of the OMZ to which it is confined (*19, 20*).

To ensure a representative history of changes in OMZ intensity, we analyzed sediment cores from three sites along the North American margin

at high temporal resolution (21). Two sites lay within the anoxic zone off Baja California (Pescadero Slope and Soledad Basin). A third is from the Southern California Bight (Santa Monica Basin), which is >1000 km north of the anoxic zone but physically connected via the coastal undercurrent (22, 23) and routinely sampled by the world's longest regional hydrographic time series, the California Cooperative Oceanic Fisheries Investigations (CalCOFI) (6). Sediment samples were taken at 0.8- to 3-mm intervals, yielding a nearly annual (1- to 2-year average) temporal resolution. All three sites contain distinct light and dark laminae indicating relatively undisturbed sediments and a lack of bioturbation. Measurements of $\delta^{15}N$ as a

function of sediment age were determined by means of ^{210}Pb chronology (fig. S1). To minimize the potential for artifacts at the core top (24), we examined sediment intervals with an age greater than 1 year (21).

During the last 50 years, all three sediment cores reveal $\delta^{15}N$ values declining gradually by nearly 1‰ between ~1960 and the mid-1980s, followed by a more rapid increase of ~1‰ since ~1990 (Fig. 2A). Given the large differences in sediment accumulation rate and composition between sites (25), the coherence in $\delta^{15}N$ suggests that they have recorded primarily large-scale oceanographic changes originating in the water column rather than in the sediments. This is corroborated

by an independent 18-year time series of sinking particulate matter $\delta^{15}N$ from sediment traps in Santa Barbara Basin, which exhibits an increasing trend similar to that of the sediment cores (Fig. 2A) (21). The timing of these decadal variations also coincides with observed changes in oxygen concentrations and nitrate deficits in hypoxic waters sampled by CalCOFI, and with changes in the volume of anoxic water in the ETNP predicted by a hindcast model for this period (10). These sedimentary $\delta^{15}N$ records provide a unique means to quantitatively test the mechanisms linking climate and anoxia in those model simulations.

To estimate the magnitude of changes in anoxia and denitrification implied by the sediment

Fig. 1. Oceanographic context of study sites. Time-mean map of O_2 (colors) at a density of Central Mode Water ($\sigma_\theta = 26.2$) whose mean depth (thin lines) shoals to the east, where anoxia is found off the equator in both hemispheres. Under anoxic conditions, oxidation of organic matter proceeds via denitrification, resulting in large regions (white lines) in which the primary N nutrient, nitrate (NO_3^-), falls below its expected covariation with phosphate (PO_4^{3-}) by more than 10 μM, as measured by the tracer N* (N* = $[NO_3^-] - 16 \times [PO_4^{3-}]$). Locations of core sites are shown with circles (blue: Santa Monica Basin; red: Pescadero; green: Soledad). Gray box defines ETNP region used for analysis of modeled and observed quantities.
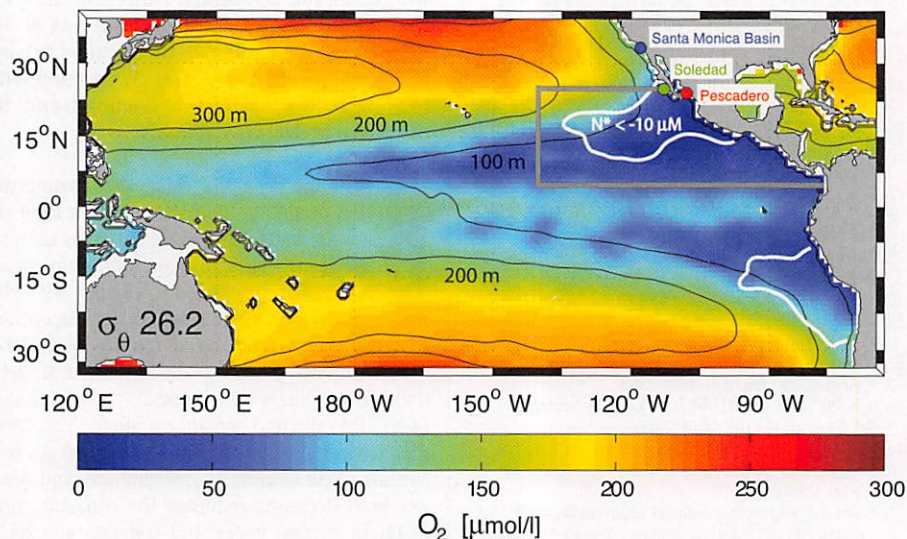

Fig. 2. Changes in sedimentary isotope ratio ($\delta^{15}N$) and its relationship to thermocline depth (Z_{tc}) in the ETNP, from data and model simulations. (A) Bulk organic $\delta^{15}N$ anomalies from three sediment core sites along the North American margin (Soledad, Pescadero, Santa Monica Basin) and from a particle flux time series in Santa Barbara Basin. Each time series is plotted as a deviation from its own time-averaged value. (B) Variations of sinking particle flux $\delta^{15}N$ in an ocean hindcast model with an explicit N cycle, forced by reconstructed atmospheric variability. The model $\delta^{15}N$ flux is averaged over the anoxic zone (125°W to coast, 5° to 25°N). A range of values is based on uncertainty in the isotopic fractionation effect (ε_{WC} = 15 to 25‰) associated with bacterial denitrification (15, 21). Thin lines are 5-year running averages of the sediment core data. (C) Relationship between thermocline depth (defined as the 13° isotherm) from World Ocean Database and sediment $\delta^{15}N$ in Pescadero sediment core, and (D) thermocline depth and particle flux $\delta^{15}N$ in model simulations. Changes in thermocline depth are averaged across the broader ETNP region (160°W to coast, 0° to 30°N). The slope of the relationship between $\delta^{15}N$ and thermocline depth in observations (-0.044 ± 0.01‰ m^{-1}; 90% confidence interval) and model simulations (-0.049 ± 0.011‰ m^{-1}) are indistinguishable.
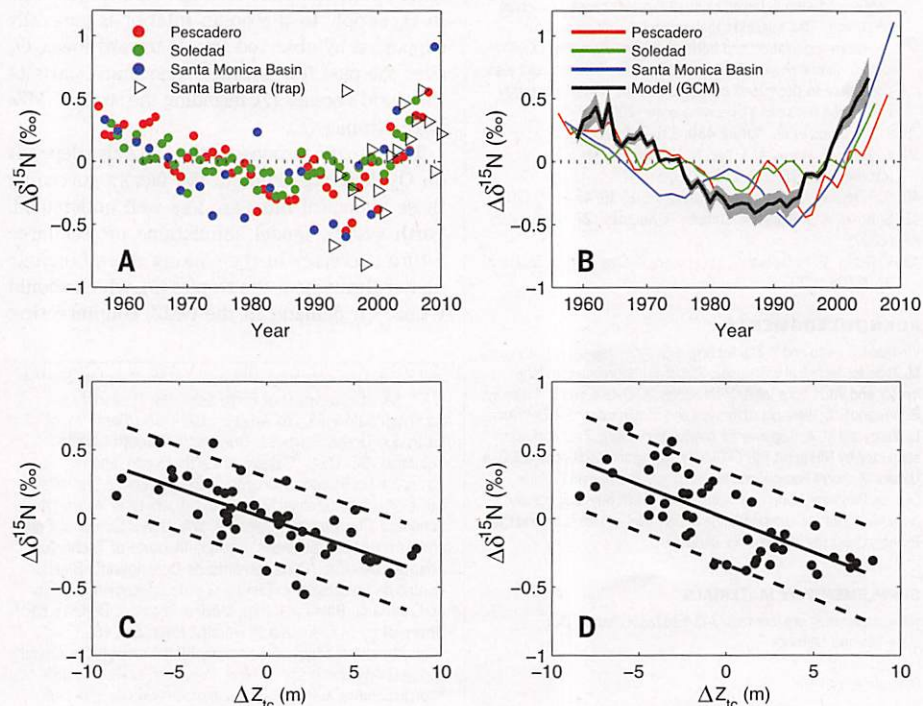
records, we directly simulate changes in sedimentary $\delta^{15}N$ in recent decades using an ocean general circulation model (GCM). The model is expanded from previous work to include an explicit cycle of N and its isotopes (21). It captures the observed structure of the tropical Pacific anoxic zone, data-based rates of denitrification (26), and the basin-scale distribution of $\delta^{15}NO_3$ (fig. S3). In response to imposed wind and buoyancy fluxes from atmospheric reanalyses from 1959 to 2005, the N cycle simulations predict large changes in anoxic water volume and integrated denitrification rates, roughly consistent with simpler stoichiometric calculations (10) (fig. S4). The decadal variations in the model-predicted $\delta^{15}N$ of particulate organic N sinking into the anoxic zone are driven by the changes in denitrification and closely match the sediment proxy data in both amplitude and timing (Fig. 2B). Additional isotopic variability arising from incomplete surface nutrient utilization is much smaller in magnitude and confined to interannual time scales (fig. S4).

The sedimentary $\delta^{15}N$ data can be used to test the hypothesized mechanisms underlying recent changes in the OMZ. According to model predictions, the decadal differences in the volume of the anoxic zone are driven by respiration rates (10, 11), which vary concurrently with the depth of the thermocline waters in which the OMZ is embedded. A shallower thermocline can increase the respiration rate in OMZ waters both by increasing surface photosynthetic production

and sinking of organic matter, and by positioning the low-O_2 waters at depths where decomposition of the sinking particles is relatively fast. We tested this relationship using historical observations from the World Ocean Database (27) to estimate changes in the depth of the 13°C isotherm (fig. S5), which lies near the core of the OMZ in the eastern tropical North Pacific. Regional variations in the thermocline depth are corrected for heat uptake, and therefore attributable to changes in ocean dynamics (21). They are strongly correlated to sedimentary $\delta^{15}N$ (Fig. 2C), and the slope of the relationship in the data is indistinguishable from that in model simulations (Fig. 2D). The coherence between modeled particulate $\delta^{15}N$ and sediment core data suggests that the $\delta^{15}N$ records are indeed a reliable proxy for large-scale changes in the intensity of the OMZ. The strong relationship to thermocline depth independently observed in model simulations and data supports the hypothesized link to climate variability, at least on decadal time scales.

The full 150-year record of sedimentary $\delta^{15}N$ measurements reveals a declining trend throughout most of the 20th century (Fig. 3A). During most of the period of climate warming, the anoxic OMZ was evidently shrinking. To determine whether the apparent long-term contraction of anoxic volume is consistent with declining O_2 demand, we extended the thermocline depth proxy back to 1850 using Intergovernmental Panel on Climate Change (IPCC) climate model reconstructions (fig. S6). These models do not directly incor-

porate oceanic observations, and thus do not reproduce the phasing or magnitude of internally generated climate variability. However, they provide a self-consistent estimate of the oceanic response to observed radiative forcing, primarily by greenhouse gases. The ~10-m deepening of the thermocline over 100 years in conjunction with a ~1‰ reduction in sediment $\delta^{15}N$ is consistent with the relationship observed over decadal time scales (Fig. 3B). The relationship between North Pacific anoxia and thermocline depth diagnosed over the last several decades thus appears to characterize the dominant climatic mechanism governing anoxic zone variability for over a century.

In the tropical Pacific, high rates of surface biological productivity and the zonal structure of the underlying thermocline are both primarily governed by the strength of surface winds, which push warm surface water to the west and draw cold, nutrient-rich deep water upward along the equator in the east. The overall rate of respiration in the tropical thermocline, and its partitioning into the intense OMZ by thermocline depth fluctuations, should therefore be closely linked to the atmospheric Walker circulation (fig. S7). Indeed, historical changes in equatorial wind stress, recorded in the zonal sea-level pressure gradient (Fig. 3C), imply a long-term weakening trend followed by a recent intensification (28–30). Both these features are reflected in thermocline depth variations and the volume of anoxia inferred from sedimentary $\delta^{15}N$. Because the oxygen content of the thermocline integrates respiration rates over multiyear residence time of regional water masses, wind and thermocline fluctuations of shorter durations are naturally filtered out of the sediment record, leaving decadal and longer time scales (31). The trends in the Pacific OMZ inferred from our $\delta^{15}N$ records originate from slowly varying strength of the tropical Walker circulation and its effect on O_2 demand, rather than changes in O_2 supply due to gas solubility and thermocline ventilation. Given the mechanistic link between equatorial wind stress and the extent of anoxia, decadal to centennial variations in the sediment $\delta^{15}N$ may provide a valuable new proxy for variations in equatorial Pacific winds and upwelling at those time scales.

Our findings demonstrate that the contemporary anoxic zone of the ETNP is currently not larger than it has been in the past 150 years, and thus cast doubt on the view that the recent expansion of the tropical Pacific OMZ is a reflection of global ocean deoxygenation driven by climate warming (8). This expansion coincides with a period of surface cooling (fig. S8) (32) and thermocline shoaling in the eastern tropical Pacific that runs counter to the prevailing climate-warming trend and partly accounts for the hiatus in global surface warming (33). It is therefore a likely manifestation of the ocean's pervasive low-frequency variability, rather than a response to rising greenhouse gases. Instead, the dominant influence of anthropogenic climate warming on tropical Pacific oxygen over the last 150 years has been the weakening of the easterly trade winds and its effect on respiratory O_2 demand. The resumption

Fig. 3. Centennial changes in Pacific OMZ denitrification and its climatic forcing.

(**A**) Sedimentary $\delta^{15}N$ from coring sites, extended back to 1850. (**B**) Trends in depth of the thermocline (13°C isotherm) in the ETNP from a database of historical temperature profiles (27) since 1955 (bold line) and from IPCC coupled climate model runs (gray line). The mean deepening across 19 individual model runs represents the response to historical radiative forcing, predominantly from greenhouse gases. The standard deviation reflects the intermodel spread as well as unforced variability, which is not in phase between models and observations. (**C**) East-west difference in sea-level pressure (ΔSLP) across the equatorial Pacific (5°N to 5°S) based on historical reconstructions (HadSLP, yellow line) and atmospheric reanalysis (ECMWF ERA40, cyan line) (39, 40). Black line is 10-year running mean of the average of the data sets. The ΔSLP is a measure of trade wind strength, with larger values indicating stronger easterly surface winds.
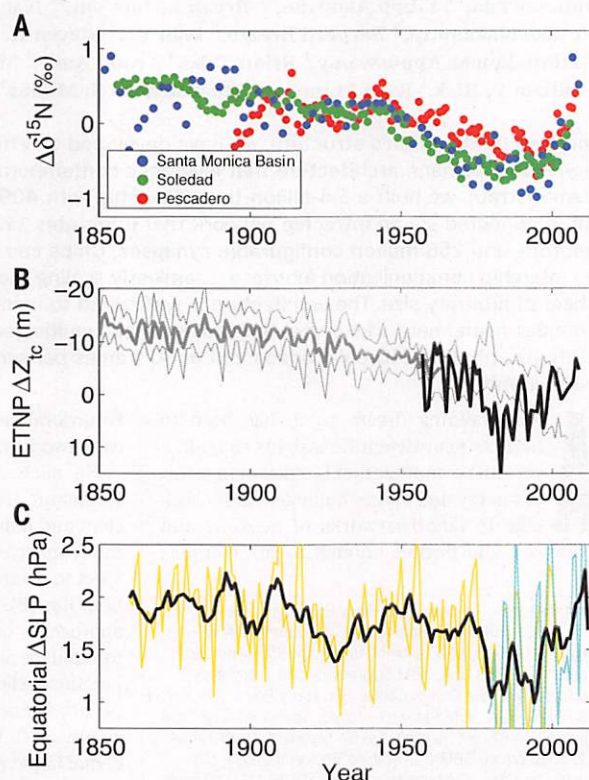
of Pacific trade wind slackening predicted under future climate warming should extend the 20th-century contraction of the OMZ into this century. This wind-driven forcing may eventually be overwhelmed by the stratification-driven deoxygenation of the ocean as a whole, as proxies of anoxia from Pleistocene sediments point to a larger tropical OMZ and greater N loss during warm climates (19, 34, 35). The relative influence of these effects and the time scales over which they operate on the tropical OMZ remain unknown.

The predominant 20th-century contraction of the North Pacific OMZ has important implications for the basin's N cycle. Over centennial time scales, the slowing pace of N loss would have reduced the NO_3^- deficit relative to plankton PO_4^{3-} requirements throughout surface waters of the N-limited North Pacific. Recent isotopic analysis of skeleton material from deep-sea corals near Hawaii also exhibit a decreasing trend over this time period, which has been interpreted as a signal of increasing N inputs from N_2 fixation (36). However, because isotopic and stoichiometric signals of denitrification are transported from the anoxic zone into the subtropical gyre (37), the reported coral trends may originate partly from the OMZ. Any remaining signal attributable to N_2 fixation would imply that the ecological niche of diazotrophs in the central gyre is uncoupled from the major N loss in the OMZ (38), and that a substantial imbalance of the Pacific N budget has persisted over the 20th century.

REFERENCES AND NOTES

1. R. Vaquer-Sunyer, C. M. Duarte, *Proc. Natl. Acad. Sci. U.S.A.* 105, 15452–15457 (2008).
2. L. Bopp, C. Le Quere, M. Heimann, A. C. Manning, P. Monfray, *Global Biogeochem. Cycles* 16, 6-1–6-13 (2002).
3. R. J. Matear, A. C. Hirst, *Global Biogeochem. Cycles* 17, 1125 (2003).
4. F. Chan et al., *Science* 319, 920 (2008).
5. R. J. Diaz, *J. Environ. Qual.* 30, 275–281 (2001).
6. J. A. Koslow, J. Couture, *Nature* 502, 163–164 (2013).
7. R. E. Keeling, A. Körtzinger, N. Gruber, *Annu. Rev. Mar. Sci.* 2, 199–229 (2010).
8. L. Stramma, G. C. Johnson, J. Sprintall, V. Mohrholz, *Science* 320, 655–658 (2008).
9. L. Bopp et al., *Biogeosciences* 10, 6225–6245 (2013).
10. C. Deutsch, H. Brix, T. Ito, H. Frenzel, L. Thompson, *Science* 333, 336–339 (2011).
11. T. Ito, C. Deutsch, *Global Biogeochem. Cycles* 27, 1119–1128 (2013).
12. S. McClatchie, R. Goericke, R. Cosgrove, G. Auad, R. Vetter, *Geophys. Res. Lett.* 37, L19602 (2010).
13. L. A. Codispoti, J. P. Christensen, *Mar. Chem.* 16, 277–300 (1985).
14. J. A. Brandes, A. H. Devol, T. Yoshinari, D. A. Jayakumar, S. W. A. Naqvi, *Limnol. Oceanogr.* 43, 1680–1689 (1998).
15. K. Kritee et al., *Geochim. Cosmochim. Acta* 92, 243–259 (2012).
16. M. A. Altabet, *J. Geophys. Res.* 94, 12771 (1989).
17. D. M. Sigman, K. L. Casciotti, in *Encyclopedia of Ocean Sciences*, J. H. Steele, K. K. Turekian, S. A. Thorpe, Eds. (Academic Press, London, 2001), vol. 4, pp. 1884–1894.
18. R. C. Thunell, D. M. Sigman, F. Muller-Karger, Y. Astor, R. Varela, *Global Biogeochem. Cycles* 18, GB3001 (2004).
19. R. S. Ganeshram, T. F. Pedersen, S. E. Calvert, G. W. McNeill, M. R. Fontugne, *Paleoceanography* 15, 361–376 (2000).
20. M. A. Altabet, M. J. Higginson, D. W. Murray, *Nature* 415, 159–162 (2002).
21. See supplementary materials on *Science* Online.
22. C. G. Castro, F. P. Chavez, C. A. Collins, *Global Biogeochem. Cycles* 15, 819–830 (2001).
23. S. S. Kienast, S. E. Calvert, T. F. Pedersen, *Paleoceanography* 17, 7-1–7-17 (2002).
24. M. F. Lehmann, S. M. Bernasconi, A. Barbieri, J. A. McKenzie, *Geochim. Cosmochim. Acta* 66, 3573–3584 (2002).
25. M. G. Prokopenko et al., *Earth Planet. Sci. Lett.* 242, 186–204 (2006).
26. T. DeVries, C. Deutsch, F. Primeau, B. X. Chang, A. H. Devol, *Nat. Geosci.* 5, 547–550 (2012).
27. J. I. Antonov, et al., in *NOAA Atlas NESDros. Inf. Serv.* 66 (U.S. Government Printing Office, Washington, DC, 2010).
28. G. A. Vecchi et al., *Nature* 441, 73–76 (2006).
29. H. Tokinaga, S.-P. Xie, C. Deser, Y. Kosaka, Y. M. Okumura, *Nature* 491, 439–443 (2012).
30. M. A. Merrifield, *J. Clim.* 24, 4126–4138 (2011).
31. T. Ito, C. Deutsch, *Geophys. Res. Lett.* 37, L03601 (2010).
32. T. M. Smith, R. W. Reynolds, T. C. Peterson, J. Lawrimore, *J. Clim.* 21, 2283–2296 (2008).
33. M. H. England et al., *Nature Clim. Change* 4, 222–227 (2014).
34. A. van Geen et al., *Paleoceanography* 18, 1098 (2003).
35. S. L. Jaccard, E. D. Galbraith, *Nat. Geosci.* 5, 151–156 (2012).
36. O. A. Sherwood, T. P. Guilderson, F. C. Batista, J. T. Schiff, M. D. McCarthy, *Nature* 505, 78–81 (2014).
37. D. M. Sigman, P. J. DiFiore, M. P. Hain, C. Deutsch, D. M. Karl, *Geophys. Res. Lett.* 36, L08605 (2009).
38. T. Weber, C. Deutsch, *Proc. Natl. Acad. Sci. U.S.A.* 111, 8741–8746 (2014).
39. R. Allan, T. Ansell, *J. Clim.* 19, 5816–5842 (2006).
40. S. M. Uppala et al., *Q. J. R. Meteorol. Soc.* 131, 2961 (2005).

ARTIFICIAL BRAINS

A million spiking-neuron integrated circuit with a scalable communication network and interface

Paul A. Merolla,[1]* John V. Arthur,[1]* Rodrigo Alvarez-Icaza,[1]* Andrew S. Cassidy,[1]* Jun Sawada,[2]* Filipp Akopyan,[1]* Bryan L. Jackson,[1]* Nabil Imam,[3] Chen Guo,[4] Yutaka Nakamura,[5] Bernard Brezzo,[6] Ivan Vo,[2] Steven K. Esser,[1] Rathinakumar Appuswamy,[1] Brian Taba,[1] Arnon Amir,[1] Myron D. Flickner,[1] William P. Risk,[1] Rajit Manohar,[7] Dharmendra S. Modha[1]†

Inspired by the brain's structure, we have developed an efficient, scalable, and flexible non–von Neumann architecture that leverages contemporary silicon technology. To demonstrate, we built a 5.4-billion-transistor chip with 4096 neurosynaptic cores interconnected via an intrachip network that integrates 1 million programmable spiking neurons and 256 million configurable synapses. Chips can be tiled in two dimensions via an interchip communication interface, seamlessly scaling the architecture to a cortexlike sheet of arbitrary size. The architecture is well suited to many applications that use complex neural networks in real time, for example, multiobject detection and classification. With 400-pixel-by-240-pixel video input at 30 frames per second, the chip consumes 63 milliwatts.

A long-standing dream (1, 2) has been to harness neuroscientific insights to build a versatile computer that is efficient in terms of energy and space, homogeneously scalable to large networks of neurons and synapses, and flexible enough to run complex behavioral models of the neocortex (3, 4) as well as networks inspired by neural architectures (5).

No such computer exists today. The von Neumann architecture is fundamentally inefficient and nonscalable for representing massively interconnected neural networks (Fig. 1) with respect to computation, memory, and communication (Fig. 1B). Mixed analog-digital neuromorphic approaches have built large-scale systems (6–8) to emulate neurobiology by using custom computational elements, for example, silicon neurons (9, 10), winner-take-all circuits (11), and sensory circuits (12). We have found that a multiplexed digital implementation of spiking neurons is more efficient than previous designs (supplementary section S3) and enables one-to-one correspondence between software and hardware (supplementary

[1]IBM Research–Almaden, 650 Harry Road, San Jose, CA 95120, USA. [2]IBM Research–Austin, 11501 Burnet Road, Austin, TX 78758, USA. [3]Cornell University, 358 Upson Hall, Ithaca, NY 14853 USA. [4]IBM Engineering and Technology Services, San Jose Design Center, 650 Harry Road, San Jose, CA 95120, USA. [5]IBM Research–Tokyo, Nippon Building Fund Toyosu Canal Front Building, 5-6-52 Toyosu, Koto-ku Tokyo 135-8511, Japan. [6]IBM T. J. Watson Research Center, 101 Kitchawan Road, Yorktown Heights, NY 10598, USA. [7]Cornell Tech, 111 Eighth Avenue No. 302, New York, NY 10011, USA.
*These authors contributed equally to this work. †Corresponding author. E-mail: dmodha@us.ibm.com